

## Vortex-Induced Rings and Gaps within Protoplanetary Disks

XIAOYI MA (马潇依)<sup>1,2</sup> PINGHUI HUANG (黄平辉)<sup>3</sup> CONG YU (余聪)<sup>4,5</sup> AND RUOBING DONG (董若冰)<sup>1,3</sup>

<sup>1</sup>*Kavli Institute for Astronomy and Astrophysics, Peking University, Beijing 100871, China*

<sup>2</sup>*Department of Astronomy, School of Physics, Peking University, Beijing 100871, China*

<sup>3</sup>*Department of Physics and Astronomy, University of Victoria, Victoria, BC, V8P 5C2, Canada*

<sup>4</sup>*School of Physics and Astronomy, Sun Yat-Sen University, Zhuhai 519082, China*

<sup>5</sup>*CSST Science Center for the Guangdong-Hong Kong-Macau Greater Bay Area, Zhuhai 519082, China*

### ABSTRACT

Observations of protoplanetary disks have revealed the presence of both crescent-shaped and ring-like structures in dust continuum emission. These crescents are thought to arise from dust-trapping vortices generated by the Rossby Wave Instability (RWI), which induces density waves akin to those caused by planets. These vortices have the potential to create gaps and rings within the disk, resulting from the dissipation of their density waves. We carry out 2D hydrodynamic simulations in the shearing box to investigate vortex-disk interaction. We find that long-lived vortices can produce dust rings and gaps in inviscid discs detectable by ALMA, and a more elongated vortex produces rings at larger separations. Vortex-induced density waves carry over two orders of magnitude higher angular momentum flux compared to planet-induced ones that shock at the same location, making the former much more effective at producing dust gaps and rings far away.

### 1. INTRODUCTION

Recent observations have revealed dust rings and gaps in protoplanetary disks (e.g., [ALMA Partnership et al. 2015](#); [Andrews et al. 2018](#); [Long et al. 2018](#)). The accumulation of dust within these rings can accelerate grain growth, making them significant sites for planetesimal formation ([Sierra et al. 2019](#)). Understanding their formation mechanisms is crucial for comprehending disk evolution and planetary formation.

Various mechanisms have been proposed to form observed rings in protoplanetary disks ([Bae et al. 2023](#)). Among them, a popular explanation is the gravitational interaction between young planets and protoplanetary disks (e.g., [Dong et al. 2015](#)). Density waves are excited by planets at Lindblad resonances, and they carry angular momentum away as they propagate. When waves dissipate, their carried angular momentum is deposited to local disk material, resulting in gap opening ([Lin & Papaloizou 1986](#)). Meanwhile, gas pressure bumps form at the inner and outer gap edges, and dust drifts towards pressure bumps to form rings ([Pinilla et al. 2012](#)).

While dozens of planets in disks have been predicted based on observed rings and gaps ([Zhang et al. 2018](#); [Bae et al. 2018](#); [Lodato et al. 2019](#)), they have largely escaped detections due to the formidable planet-to-star flux ratios ([Asensio-Torres et al. 2021](#)). Whether planets are responsible for the majority of dust rings and gaps remains debated ([Jiang & Ormel 2021](#)). In addition, dust rings and gaps have been found in disks so young that the local material has only had time to complete on the order of 1,000 orbits ([Segura-Cox et al. 2020](#)). Whether planets can form and generate disk structures so quickly remains unclear.

In this study, we aim to explore a novel and non-planetary mechanism for generating dust rings and gaps in disks through vortex-disk interactions. Vortices are anticyclonic structures characterized by gas streamlines revolving around their center. They may form through the Rossby Wave Instability (RWI), initially identified via linear analysis ([Lovelace et al. 1999](#); [Li et al. 2000](#)) and further explored in its nonlinear evolution through simulations ([Li et al. 2001](#); [Meheut et al. 2013](#)). RWI is triggered by rapid radial variations in vortensity in low-turbulence discs. Such conditions may be realized at edges of gaps ([Zhu et al. 2014](#); [Miranda et al. 2017](#)) or narrow rings ([Lovelace et al. 1999](#); [Li et al. 2000](#)). Vortices can trap dust particles sufficiently and concen-

trate solids at their center (Meheut et al. 2012b; Meheut 2013a,b), resulting in crescent-shaped structures observable in continuum emission (Birnstiel et al. 2013; Baruteau & Zhu 2016). Such structures have been found in many disks (van der Marel et al. 2013, 2020; Casassus et al. 2013).

In disks, vortices can induce velocity perturbations, and excite spiral density waves (Li et al. 2001; Meheut et al. 2013). While previous works have focused on the excitation of the RWI and the subsequent vortex formation, this study takes a step forward by investigating the substructures that emerge from vortex-disk interactions. Similar to the ones excited by planets, vortex-induced density waves may also propagate and dissipate, leading to gap opening. Candidate vortices and dust rings have been found to coexist in some disks, such as HD 135344B (van der Marel et al. 2016) and HD 143006 (Pérez et al. 2018; Andrews et al. 2018), promoting the hypothesis that the two may be physically related.

We carry out hydrodynamics simulations to study the interactions between a non-migrating vortex and an inviscid disk. The paper is organized as follows. We introduce our simulations in §2 and present their results in §3, before discussing our findings in §4. We summarize the main finding in §5.

## 2. METHOD

We conduct 2D hydrodynamics simulations of protoplanetary disks in the shearing box using the Athena++ code (Stone et al. 2020) to examine the propagation and dissipation of vortex-generated density waves, as well as the subsequent gap-opening process. We employ the simulations for isothermal disks. Viscosity, self-gravity and magnetic field are not included, and their effects will be discussed in §4.2. The numerical setup, the initial conditions, and the boundary conditions are specified in §2.1, §2.2, and §2.3, respectively, with a list of models in Table 1.

### 2.1. Numerical Setup

The shearing box approximation (Narayan et al. 1987; Stone & Gardiner 2010) adopts a frame of reference at the radius  $r_0$  co-rotating with the disk at the orbital velocity  $\Omega_0 = \Omega(r_0)$ . In this frame, we define a Cartesian coordinate system  $(x, y, z)$  with the unit vector  $(\hat{\mathbf{i}}, \hat{\mathbf{j}}, \hat{\mathbf{k}})$  as:

$$\begin{aligned} x &= r - r_0 \\ y &= r_0(\phi - \Omega_0 t) \\ z &= z \end{aligned} \quad (1)$$

where  $(r, \phi, z)$  are cylindrical coordinates. The orbital motion in the shearing box is approximated by a linear function as  $-q\Omega_0 x \hat{\mathbf{j}}$ , where the shearing parameter  $q$  is defined as:

$$q \equiv -\frac{d \log \Omega}{d \log r} \quad (2)$$

For Keplerian flow,  $q = 3/2$ . The 2D hydrodynamical equations are written in the co-rotating Cartesian coordinate system as:

$$\frac{\partial \Sigma_{\text{gas}}}{\partial t} + \nabla \cdot [\Sigma_{\text{gas}} \mathbf{v}_{\text{gas}}] = 0, \quad (3)$$

$$\begin{aligned} \frac{\partial \Sigma_{\text{gas}} \mathbf{v}_{\text{gas}}}{\partial t} + \nabla \cdot [\Sigma_{\text{gas}} \mathbf{v}_{\text{gas}} \mathbf{v}_{\text{gas}} + P] = \\ \Sigma_{\text{gas}} \Omega_0^2 (2qx \hat{\mathbf{i}}) - 2\Omega_0 \hat{\mathbf{k}} \times \Sigma_{\text{gas}} \mathbf{v}_{\text{gas}} \end{aligned} \quad (4)$$

where 4 are the gas continuity and momentum equation, respectively, where  $\Sigma_{\text{gas}}$  is the gas surface density,  $\mathbf{v}_{\text{gas}}$  is the gas velocity and  $P$  is the gas pressure. For isothermal disks,  $P = c_s^2 \Sigma_{\text{gas}}$ , where  $c_s$  is isothermal sound speed.

We include a dust fluid module in the Athena++ (Huang & Bai 2022) by treating dust as pressureless fluid. The continuity and momentum equations for dust are defined as follows:

$$\frac{\partial \Sigma_{\text{dust}}}{\partial t} + \nabla \cdot [\Sigma_{\text{dust}} \mathbf{v}_{\text{dust}}] = 0, \quad (5)$$

$$\begin{aligned} \frac{\partial \Sigma_{\text{dust}} \mathbf{v}_{\text{dust}}}{\partial t} + \nabla \cdot [\Sigma_{\text{dust}} \mathbf{v}_{\text{dust}} \mathbf{v}_{\text{dust}}] = \\ \Sigma_{\text{dust}} \Omega_0^2 (2qx \hat{\mathbf{i}}) - 2\Omega_0 \hat{\mathbf{k}} \times \Sigma_{\text{dust}} \mathbf{v}_{\text{dust}} + \Sigma_{\text{dust}} \frac{\mathbf{v}_{\text{gas}} - \mathbf{v}_{\text{dust}}}{t_s} \end{aligned} \quad (6)$$

The symbols are defined similarly to the gas fluid. The stopping time,  $t_s$ , represents the timescale over which the velocity of dust particles exponentially decays due to aerodynamic drag. We only include one dust species with a Stokes number  $St = 0.1$ , neglecting dust feedback and diffusion. The Stokes number  $St$  of dust particles in the Epstein regime is:

$$St = \frac{\pi s \rho_{\text{m,dust}}}{2 \Sigma_{\text{gas}}} \quad (7)$$

where  $s$  is the size of the dust particle and  $\rho_{\text{m,dust}}$  is the material density of the dust particle. While  $St$ , instead of  $s$ , is fixed in our simulations, the gas surface density  $\Sigma_{\text{gas}}$  varies only on the order of 10%, resulting in a near-constant  $s$ .

We utilize the second-order piecewise linear method (PLM) spatial reconstruction and the Van-Leer 2 (VL2)

time integrator, the HLLC Reimann solver for gas and the default Reimann solver for dust (Huang & Bai 2022) in this study. To reduce computational costs, we incorporate the orbital advection algorithm to speed up the azimuthal calculations and reduce the truncation errors. (Masset 2000; Stone et al. 2020).

The grid is uniformly spaced, and the cells are squared. Based on the convergence test in Appendix A, a resolution of 256 cells per disk scale height ( $h$ ) is required to accurately model weak density wave propagation and shocks in an inviscid environment. This is in line with previous results (Dong et al. 2011b), as lower resolutions may lead to numerical diffusion and premature wave dissipation.

All simulations are carried out for a minimum of 400 orbits, corresponding to 0.4 Myr at a distance of 100 AU around a solar mass star.

## 2.2. Initial conditions

Our main goal is to study vortex-disk interaction rather than the vortex-formation process. While the RWI can be triggered in a variety of scenarios, such as at the dead zone edge (Miranda et al. 2017) or at the edge of planetary gaps (Zhu et al. 2014), we choose to trigger RWI by introducing a Gaussian surface density bump to the uniform background density, following Ono et al. (2018). This method generates vortices akin to those produced by other mechanisms. We adopt this approach as it allows us to isolate the vortex-disk interaction from other complications, such as viscosity variation near the dead zone and density waves induced by planets.

The initial gas surface density profile is given by:

$$\Sigma_{\text{gas}}(x, y) = \Sigma_{\text{gas},0} \left( 1 + A_0 e^{-\frac{1}{2} \left( \frac{x-x_0}{\Delta w_0} \right)^2} \right) \quad (8)$$

where  $\Sigma_{\text{gas},0} = 1$  is the uniform background profile. The initial dust surface density follows the gas with a uniform dust-to-gas ratio of 0.01. The gas background profile is characterized by three parameters:  $A_0$  for the density contrast of the bump,  $\Delta w_0$  for its radial half-width, and  $x_0$  for the location of the bump center.

We fix  $x_0 = 0$  and  $w_0 = 0.632h$ . Here,  $h = c_s/\Omega_0 = 0.1$ , with  $\Omega_0 = 1$  and isothermal sound speed  $c_s = 0.1$  in code units. We explore the parameter space for  $A_0$  (column 1 in Table 1) using four disk models. Each model corresponds to a most unstable azimuthal mode,  $m_*$  (column 4 in Table 1). These values are determined through linear analysis of RWI (Ono et al. 2016, 2018).

The initial velocities are set by hydrostatic equilibrium:

$$v_{\text{gas},x,0} = 0 \quad (9)$$

$$v_{\text{gas},y,0} = -q\Omega_0 x + \frac{1}{2\Omega_0 \Sigma_{\text{gas}}} \frac{dP}{dx} \quad (10)$$

In addition, we impose a small initial gas velocity perturbation in  $x$  according to the most unstable azimuthal mode  $m_*$  to trigger the RWI:

$$\delta v_{\text{gas},x,0} = 10^{-5} \cos(m_* y) e^{-\frac{1}{2} \left( \frac{x}{0.1} \right)^2} \quad (11)$$

## 2.3. Domain size and boundary conditions (BC)

The simulation domain in the  $x$  direction ( $x_{\min}, x_{\max}$ ) (column 2 in Table 1) is set to fully capture the shock dissipation for all disk models, which will be elaborated in §3.3.

The simulation domain in the  $y$  direction ( $y_{\min}, y_{\max}$ ) (column 3 Table 1) is determined by its most unstable azimuthal mode  $m_*$ . According to Ono et al. (2018), the number of primary vortices formed equals  $m_*$ , which later merges into a single vortex. To avoid complications associated with vortex merging, we truncate the full azimuthal domain to  $1/m_*$ , leaving only one vortex within the domain throughout the simulation.

The boundary condition (BC) is periodic in the  $x$  direction and shearing periodic in the  $y$  direction. To minimize the wave reflection along  $x$  edges, we add a wave-damping zone along the  $x$  boundaries to gradually damp all variables  $X$  (gas and dust density, and velocities) to the initial values by the following equation (Huang & Bai 2022):

$$\frac{\partial X}{\partial t} = \zeta_{\text{dr}} \Omega_0 [X(t=0) - X] \left( \frac{|x - x_{\text{damping}}|}{\Delta x_{\text{damping}}} \right)^2, \quad (12)$$

where  $\zeta_{\text{dr}}$  is the damping rate, which we set to be 100, and  $x_{\text{damping}}$  denotes the damping edge, defined as  $x_{\text{damping}} = 0.89x_{\max}$  for the outer boundary and  $x_{\text{damping}} = 0.89x_{\min}$  for the inner boundary.  $\Delta x_{\text{damping}}$  represents the width of the damping zone, which is  $\Delta x_{\text{damping}} = 0.11|x_{\max}|$  for the outer boundary and  $\Delta x_{\text{damping}} = 0.11|x_{\min}|$  for the inner boundary.

## 3. RESULT

We start from the model with the lowest initial bump amplitude (Model A4), showing gap opening in §3.1 and wave dissipation in §3.2. We then move on to other models in Table 1 and examine how vortex-disk interactions

**Table 1.** List of Disk Models

	Initial Setup <sup>a</sup>			Model Characteristics <sup>b</sup>						Planet Analog <sup>c</sup>	
Column	1	2	3	4	5	6	7	8	9	10	11
Name	Bump Amplitude	Simulation Domain		Most Unstable Mode	Characteristic Time	Aspect Ratio	Wave Amplitude	AMF	Ring Position	Planet mass	
	$A_0$	$(x_{\min}, x_{\max})$	$(y_{\min}, y_{\max})$	$m_*$	$\tau_{20}$	$\chi_v$	$(\delta\Sigma_{\text{gas}})_{\text{max}}$	$F_J$	$x_{\text{ring}}$	$M_{\text{p,shock}}$	$M_{\text{p,AMF}}$
Epoch				$t = \tau_{20}$		$t = 20$ orbits	$t = 20$ orbits	$t = \tau_{20}$			
Unit	$[\Sigma_{\text{gas},0}]$	$[h]$	$[h]$	[orbits]		$[\Sigma_{\text{gas},0}]$	$(\times 10^{-5})$	$[h]$	$[M_{\text{th}}]$	$[M_{\text{th}}]$	
A1	0.439	$[-20, 20]$	$[-10\pi/4, 10\pi/4]$	4	149	4.00	0.25	2.87	8.16	0.011	0.176
A2	0.358	$[-20, 20]$	$[-10\pi/4, 10\pi/4]$	4	210	4.61	0.18	1.40	9.15	0.006	0.123
A3	0.227	$[-30, 30]$	$[-10\pi/3, 10\pi/3]$	3	461	5.99	0.14	0.61	12.33	0.002	0.081
A4	0.205	$[-30, 30]$	$[-10\pi/3, 10\pi/3]$	3	860	8.28	0.04	0.10	16.88	0.001	0.034

<sup>a</sup>: The initial setup of the models is described by the density contrast amplitude of the initial bump ( $A_0$ ) and simulation domain ( $(x_{\min}, x_{\max}), (y_{\min}, y_{\max})$ ).

<sup>b</sup>: The parameters that characterized the models are the following (see §3.3):

- $m_*$ : the most unstable mode of RWI calculated by Ono et al. (2016, 2018)
- $\tau_{20}$ : characteristic time when  $\langle \delta\Sigma_{\text{dust}}/\Sigma_{\text{dust},0} \rangle_y \sim 20$  at the location of dust ring B
- $\chi_v$ : aspect ratio of the vortex measured at  $t = \tau_{20}$
- $(\delta\Sigma_{\text{gas}})_{\text{max}}/\Sigma_{\text{gas},0}$ : peak wave amplitude at its shock location when it is initially excited at  $t = 20$  orbits
- $F_J$ : angular momentum flux carried by the wave at  $t = 20$  orbits
- $x_{\text{ring}}$ : location of the ring further away from the vortex at  $t = \tau_{20}$

<sup>c</sup>:  $M_{\text{p,shock}}$  and  $M_{\text{p,AMF}}$  are the masses of the planet that excites waves which shock at the same location and carry the same amount of AMF as the vortex (see §3.4).

depend on vortex properties in §3.3. Finally, we compare the locations of the gaps opened by vortices and planets, as well as the angular momentum flux carried by their density waves in §3.4.

### 3.1. Density wave excitation and gap opening by the vortex

Figure 1 presents snapshots of the gas (left) and dust surface density (right) for **Model A4** in Table 1, illustrating the evolution of the system. At the start of the simulation, the gas density bump undergoes RWI. A vortex (black solid arrow, left column) then forms within tens of orbits. One vortex excites a pair of density waves (black dashed arrow, left column) on each side<sup>1</sup>, typically with low contrasts ( $\sim 10\%$  in this case), as shown in Huang et al. (2019). A gas gap (white dashed arrow, left column) gradually forms on each side as the waves dissipate, prompting the formation of two pressure bumps at its two edges.

Due to the aerodynamic gas drag, dust particles drift towards the pressure bumps and vortex. A dust gap

is opened at the location of the gas gap, and two dust rings (white solid arrow and white dotted arrow, right column) form at its two pressure bumps. The gas gap deepens and widens with time, pushing the two dust rings further apart.

The central position of the gas (and dust) gap remains relatively unchanged. As there is one gap on each side of the vortex, in total there are two gaps and four dust rings in our simulation domain. The two dust rings closer to the vortex (dust ring A; white dotted arrow, right column) move towards each other and may eventually merge into the vortex, as observed in the models with higher initial density contrast  $A_0$  (see §3.3). We will only focus on the dust ring further away from the vortex (dust ring B; white solid arrow, right column).

### 3.2. Shock Development and Wave Dissipation

We investigate the origin of the gaps in **Model A4** by studying the propagation and dissipation of the density waves excited by the vortex.

We calculate the angular momentum flux (AMF) carried by the density wave (Miranda & Rafikov 2020):

$$F_J(x) = \int_{y_{\min}}^{y_{\max}} \Sigma_{\text{gas}}(x, y) v_{\text{gas},x}(x, y) \delta v_{\text{gas},y}(x, y) dy, \quad (13)$$

<sup>1</sup> The two waves on each side are symmetric if the vortex is symmetric (Huang et al. (2019) Figure 1). In our simulations with periodic BC in  $y$ , since the vortex is as long as the simulation domain, the two waves overlap.



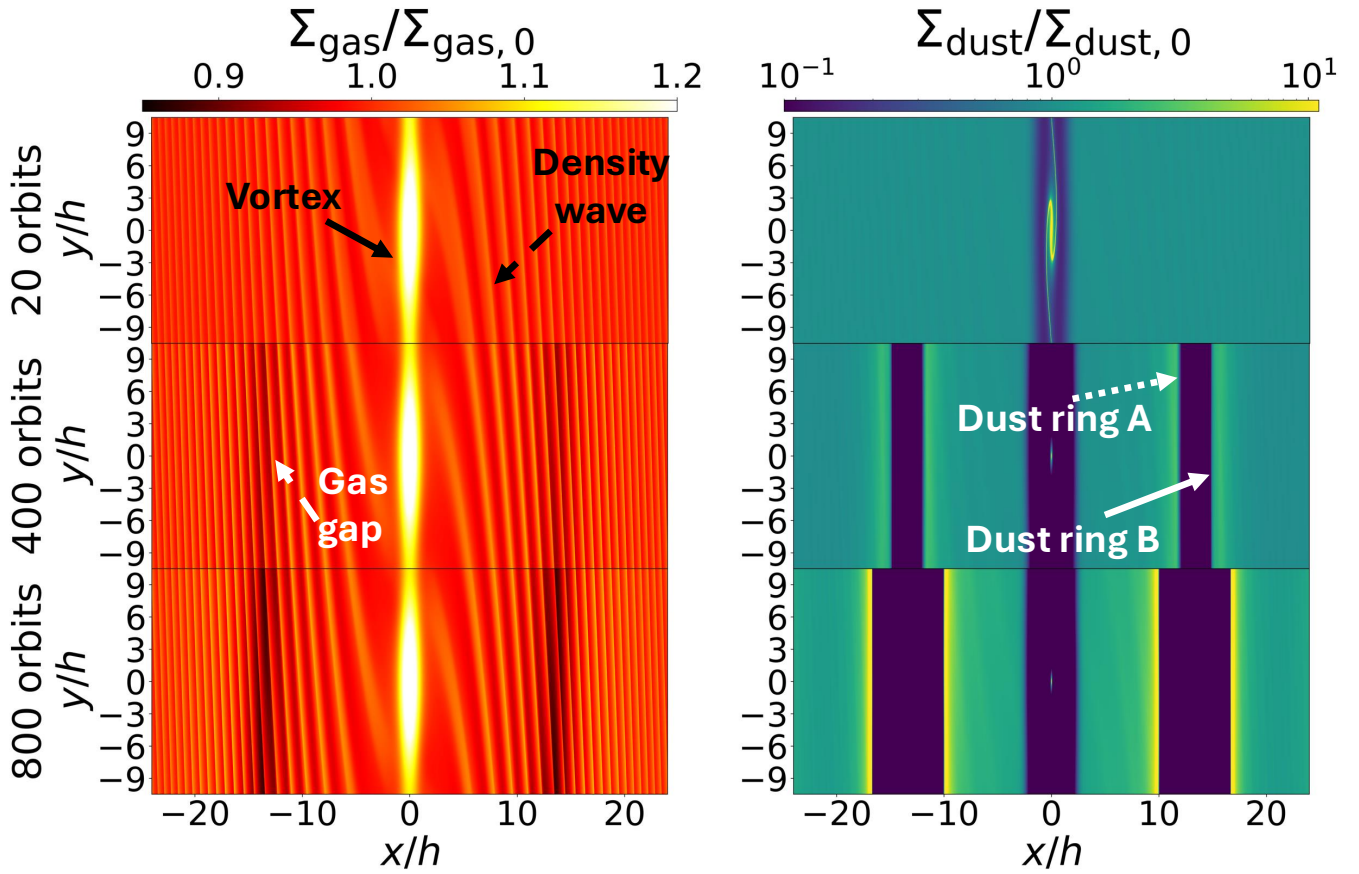


**Figure 1.** Surface density snapshots for gas (left) and dust (right) of module with lowest initial bump amplitude (Model A4), at  $t = 20, 400$  and  $800$  orbits. An RWI vortex centred at  $(x, y) = (0, 0)$  forms (black solid arrow, left column), generating spiral density waves (black dashed arrow, left column). As the system evolves, a gas gap is opened on each side of the vortex (white dashed arrow, left column), prompting the formation of two dust rings at its two edges (dust ring A and B; white dotted arrow and white solid arrow, right column). The gas gap deepens and widens with time, pushing the dust rings further apart. See §3.1 for details.

where  $v_{\text{gas},x}(x, y)$  is the radial velocity and  $\delta v_{\text{gas},y}(x, y) = v_{\text{gas},y}(x, y) - v_{\text{gas},y,0}(x, y)$  is the azimuthal velocity perturbation. The total AMF acquired by the wave during its excitation is determined by vortex-disk interactions and is a characteristic of the vortex. Before the wave shocks, its AMF remains constant. Once it shocks, the angular momentum carried by the wave is gradually transferred to the local disk, causing the AMF to decay with distance  $x$  (Goodman & Rafikov 2001), as illustrated in Figure 2(c). Where the AMF starts to decay thus indicates the shock location. As this transfer of angular momentum causes gap opening, the AMF acquired by the wave prior to dissipation sets its total gap opening ability.

The shock location can also be identified by searching for the jump in *potential vorticity*, also known as *vortensity* (Cimerman & Rafikov 2021):

$$\zeta \equiv \frac{(\nabla \times \mathbf{v}_{\text{gas}})_z}{\Sigma_{\text{gas}}}. \quad (14)$$

Vortensity remains conserved in inviscid and barotropic environment, except at shock locations, where vortensity is excited (Kevlahan 1997; Li et al. 2005).

Figure 2 displays the azimuthally averaged radial profiles of normalized gas surface density (panel (a)), dust surface density (panel (b)), AMF carried by the density waves (panel (c)), and vortensity (panel (d)) for Model A4 at  $800$  orbits. Since the shearing box is symmetric with respect to the  $y$  axis, we will focus on discussing one side of the simulation.

The gas gap is situated at a distance of  $13.6h$  from the vortex, denoted by the black dashed line. There are two narrow dust rings (yellow dash lines, panel (b)) at the two pressure bumps at the gap edges. Dust ring A (dotted arrow, panel (b)) located  $9.9h$  away from the vortex and dust ring B (solid arrow, panel (b)) is  $16.9h$  away. The gas gap location (black dashed line, panel (a)) aligns with the jump in vortensity (black dashed line,

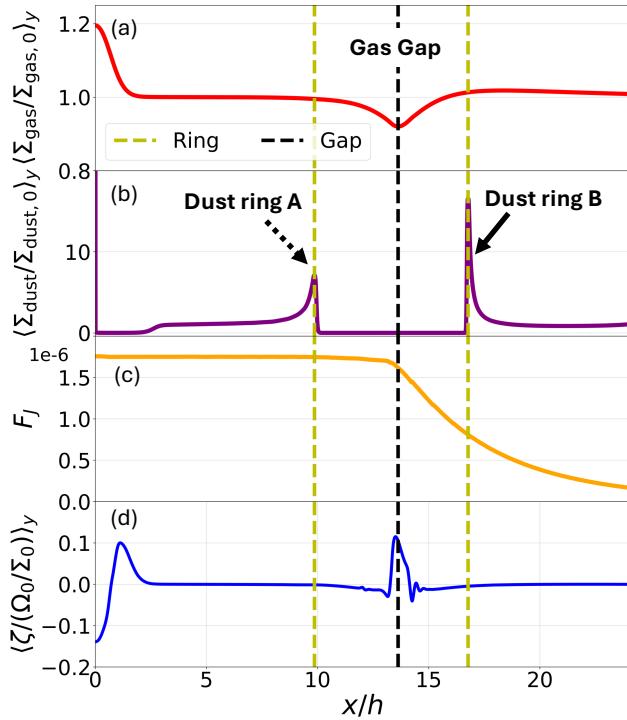


**Figure 2.** The azimuthally averaged radial profiles for the gas (a) and dust surface density (b), the angular momentum flux carried by the waves (c), and vortensity (d) for Model A4 at  $t = 800$  orbits (bottom panels in Figure 1). Since the shearing box is symmetric with respect to the  $y$  axis, this image only displays the profiles for  $x > 0$ . The peaks at  $x/h = 0$  in panels (a) and (b) are over-densities at the center of the vortex. The black dashed line at  $x = 13.6h$  marks the location of the gas gap trough (a), the starting point of the AMF decay (c), and the vortensity peak (d), indicating the shock in the wave. The two yellow dashed lines indicate the locations of the two dust rings in panel (b). We will focus on dust ring B that is located at  $16.9h$  away from the vortex (solid arrow).

panel (d)), and the starting point of the AMF decay (black dashed line, panel (c)), indicating that the gas gap is indeed opened by wave dissipation caused by the shock. We thus conclude that a vortex can create rings and gaps through its density waves.

Next, we examine the azimuthal wave profiles,  $\delta\Sigma_{\text{gas}} = \Sigma_{\text{gas}} - \Sigma_{\text{gas},0}$  as a function of  $y$  at a few different  $x$ , for Model A4 in Figure 3. The profiles are aligned by their peaks  $y_{\text{peak}}$ . We choose an early frame at  $t = 20$  orbits to minimize the influence of gap opening. As the density wave travels radially away from the vortex, its amplitude increases with distance  $x$  as  $x^{1/2}$  due to the conservation of AMF (Goodman & Rafikov 2001). To compensate for this, we normalize the wave profiles by  $x^{1/2}$ . The leading edge of the wave gradually steepens, and becomes nearly vertical at  $x = 13.6h$ , where

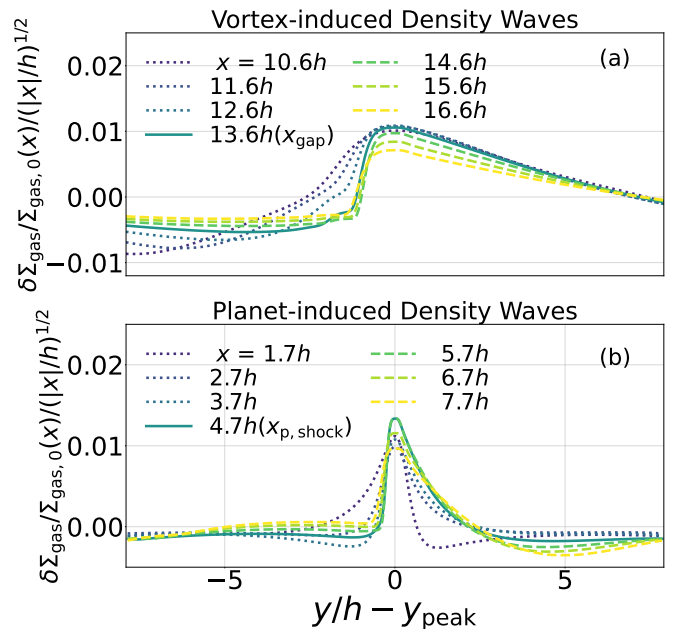


**Figure 3.** Panel (a): Azimuthal profiles for vortex-induced density wave of Model A4 at  $t = 20$  orbits (top left panel in Figure 1). The shock location is identified in Figure 2 (black dashed line) as  $x_{\text{gap}} = 13.6h$ . The profiles are depicted at seven radii ( $x$ ), including three pre-shock locations ( $10.6h$ ,  $11.6h$  and  $12.6h$ ) (dotted lines), one shock location (solid line), and three post-shock locations ( $14.6h$ ,  $15.6h$  and  $16.6h$ ) (dashed lines). (b): Azimuthal profiles for planet-induced density waves ( $M_{\text{p}} = 0.01M_{\text{th}}$ ) at  $t = 20$  orbits. The shock location  $x_{\text{p,shock}} = 4.7h$  is calculated using Equation 16. The profiles are depicted at seven radii ( $x$ ), including three pre-shock locations ( $1.7h$ ,  $2.7h$  and  $3.7h$ ) (dotted lines), one shock location (solid line), and three post-shock locations ( $5.7h$ ,  $6.7h$  and  $7.7h$ ) (dashed lines).

the wave shocks. Before that, the  $x^{1/2}$ -normalized wave amplitude is conserved; after that, the amplitude drops due to wave dissipation. The excitation–shock–dissipation process of the waves generated by a vortex resembles that of the waves generated by a planet (Muto et al. 2010; Dong et al. 2011a). However, the two types of waves have different profiles, with the planet induced ones having a full-width-half-magnitude  $\sim 70\%$  smaller, and slightly increase in wave amplitude when the wave shocks (Figure 3(b)). In Section 3.4, we compare the properties of waves excited by vortices with those excited by planets.

### 3.3. Comparative Analysis of Vortex Properties and Substructures in Disk Models

We analyze vortex and ring properties in different models (Table 1) to identify the correlation between the vortex aspect ratio and the location of the dust ring.

From now on, “dust ring” specifically refers to dust ring B (white solid arrow, Figure 1), the one further from the vortex, unless otherwise specified.

Models with a lower initial surface density contrast  $A_0$  produce more elongated vortices (blue ellipse, left column in Figure 4), quantified by the aspect ratio  $\chi_v$  (column 6 in Table 1) as defined in Appendix B. Such vortices excite density waves with lower amplitudes  $((\delta\Sigma_{\text{gas}})_{\text{max}})$ ; column 7 in Table 1) and that carry less AMF ( $F_J$ ; column 8 in Table 1). These waves shock at larger distances (Goodman & Rafikov 2001), producing gaps and rings ( $x_{\text{ring}}$ ; column 9 in Table 1) further away from the vortex (Figure 4). This trend is further illustrated in Figure 5, showing the locations of the gaps and rings in azimuthally averaged surface density profiles. More quantitatively, Figure 6 shows that  $\chi_v$  is in a tight linear correlation ( $\chi^2 = 0.007$ ) with  $x_{\text{ring}}$ , the location of the dust ring in the pair produced by each gas gap (solid arrows in Figure 5, bottom):

$$x_{\text{ring}}/h = a\chi_v - b, \quad (15)$$

where  $a = 2.07 \pm 0.06$  and  $b = -0.2 \pm 0.3$ .

### 3.4. Comparison with Planet-disk Interaction

Both planets and vortices can excite density waves that propagate in disks, which shock and dissipate at certain distances to open gaps. However, the profiles of the two categories of waves are not the same. This is evident by comparing panel (a) with panel (b) in Figure 3, which shows the evolution of weak waves induced by a sub-thermal mass planet. As the propagation of planet-induced waves and the associated gap opening process have been thoroughly studied (Goodman & Rafikov 2001; Dong et al. 2011a,b), we hope to compare the two to help us understand vortex-induced waves. Specifically, we determine the mass of the corresponding planets whose waves shock at the same distance, or carry the same AMF, as those induced by the vortex.

In Figure 7(a) we show the mass of the planet whose primary density wave<sup>2</sup> shock at the same distance as vortex-induced wave for each of our models using the relation found by Goodman & Rafikov (2001):

$$M_{\text{p,shock}} \approx \left( \frac{|x|_{\text{shock}}}{0.8h} \right)^{-5/2} \left( \frac{12/5}{\gamma + 1} \right) M_{\text{th}} \quad (16)$$

<sup>2</sup> A low mass planet can excite multiple density waves that shock at different locations (Dong et al. 2017; Bae & Zhu 2018). Here we refer to the primary wave with the shortest shock length.

where  $|x|_{\text{shock}}$  is the shock length of the vortex-induced wave, corresponds to the location of the gas gap (See §3.2 for details),  $\gamma = 5/3$  is the adiabatic index and  $M_{\text{th}} = c_s^3/G\Omega_p$  is the disk thermal mass (Goodman & Rafikov 2001; Dong et al. 2011a). For a disk with  $h/r = 0.1$  around a solar mass star at the planetary location, the thermal mass will be roughly 1 Jupiter mass (Miranda & Rafikov 2019). Vortices in all our models correspond to sub-thermal mass planets ( $M_{\text{p,shock}} \ll M_{\text{th}}$ ), while less elongated vortices correspond to more massive planets.

Since waves excited by a planet and a vortex differ in profile, those with the same shock length may carry different AMF. In Figure 7(b) we find the mass of the planet whose density waves carry the same AMF as vortex-induced ones ( $F_J$ ; column 8 in Table 1) for each of our models using the relation in Equation 17 (Dong et al. 2011a):

$$M_{\text{p,AMF}} \approx \left( \frac{F_J \Omega_p}{0.93 \Sigma_0 r_p c_s^3} \right)^{1/2} M_{\text{th}}. \quad (17)$$

Observationally, the waves excited by such a planet have the same gap opening potential as the ones excited by the corresponding vortex. Less elongated vortices that generate density waves with higher AMF correspond to more massive planets.

Combining two panels in Figure 7, we see that  $M_{\text{p,AMF}}$  can be one order of magnitude higher than  $M_{\text{p,shock}}$ . For a planet whose waves shock at the same distance as those induced by a vortex, the AMF carried by the vortex-induced waves (orange dots, Figure 8) can be two orders of magnitude higher than the AMF carried by the planet-induced waves (blue dots, Figure 8), indicating the greater gap-opening ability of the vortex compared with the planet.

## 4. DISCUSSION

In this section, we compare the synthetic image of vortex-disk interaction with real observations (§4.1) and discuss the impact of physical effects not considered in our study (§4.2).

### 4.1. Comparison with Real Observation

While recent observations have revealed that several disks exhibit azimuthal asymmetries (van der Marel et al. 2020), only a few disks hold both asymmetries and dust rings, such as HD 135344B (Figure 9(c); Cazzoletti et al. 2018).

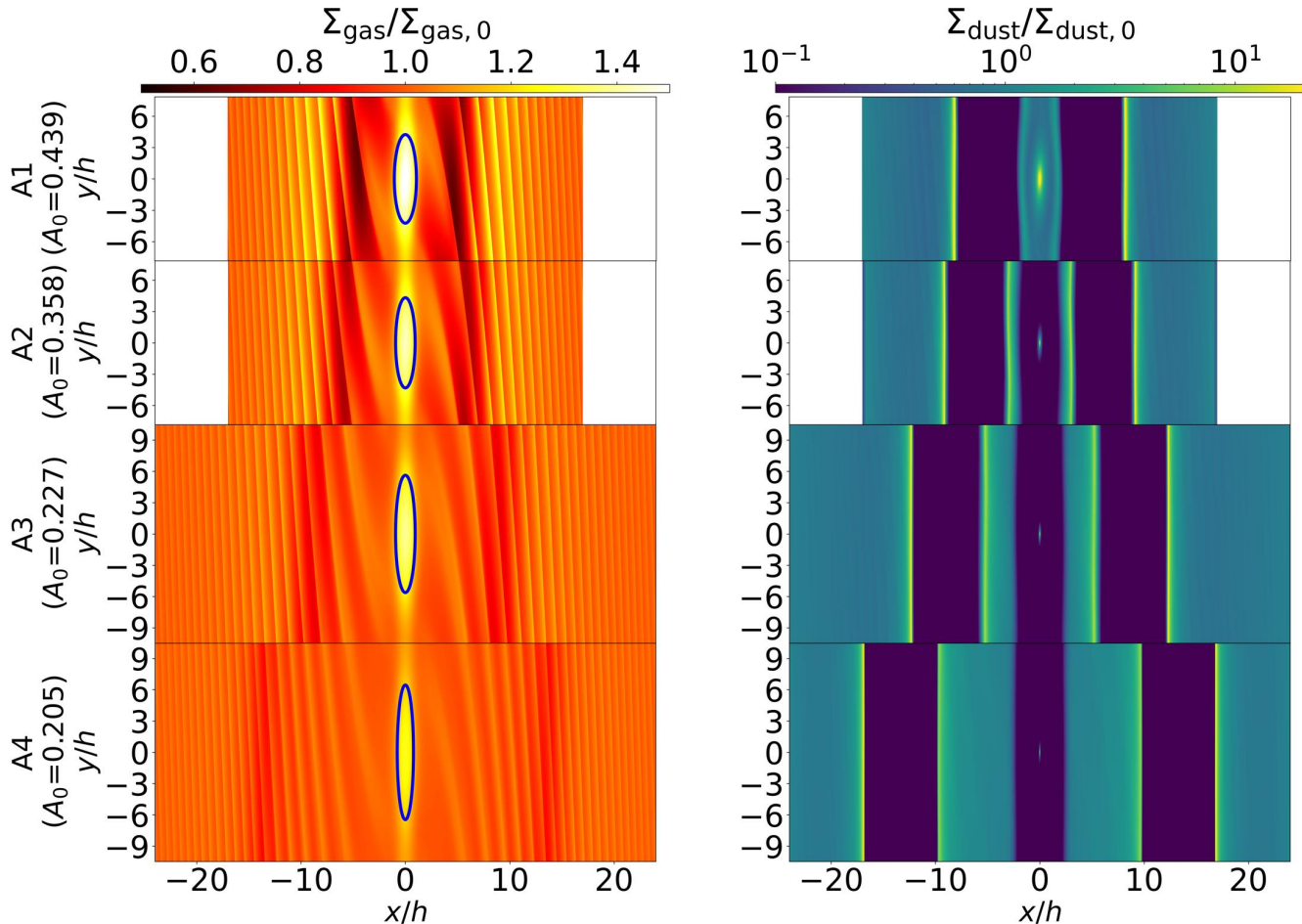


**Figure 4.** Surface density for gas (left) and dust (right) at  $t = \tau_{20}$  for disk models listed in Table 1. The blue ellipse delineates the edge of the vortex core. Models with a lower initial density contrast  $A_0$  exhibit more elongated vortices, excite density waves with lower amplitudes that shock at larger distances, and produce gaps and rings situated further away from the vortex.

HD 135344B features an inner dust cavity, an inner ring and an outer azimuthal asymmetry in dust continuum. Our synthetic image (Figure 9(b)), created as described in Appendix C, resembles these observed features, suggesting the vortex may have produced the inner dust ring.

#### 4.2. Other Physical Effects

Our simulations exclude physical effects such as vortex migration, viscosity, radiative cooling, self-gravity, 3D dynamics, and dust feedback. Below, we discuss how these factors may influence the contrast of vortex-induced substructures and the vortex lifetime.

##### 4.2.1. Contrast of Vortex-Induced Substructures

While our simulations assume an inviscid disk, viscous processes can influence the gap-opening process by smoothing disk structures, thereby counteracting gap

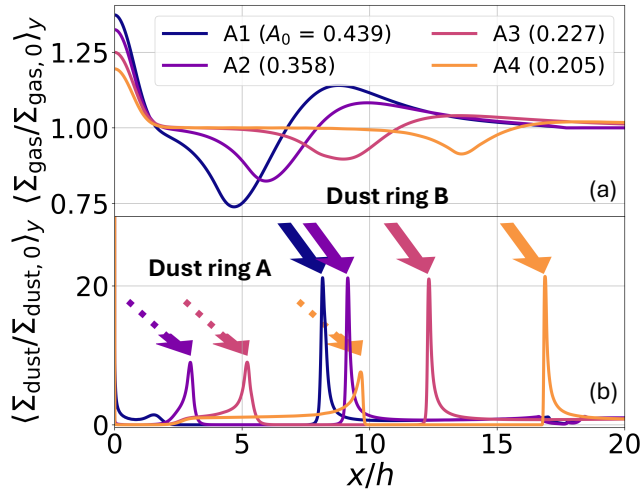
formation (Fung et al. 2014). Thus, the density contrast of the rings and gaps in a viscous disk would be shallower compared with those within Figure 1 and Figure 4.

Figure 9 shows a synthetic image from a simulation for a locally isothermal disk. In disks with finite cooling times, the density contrast of rings and gaps varies with the cooling timescales of the disks. This could cause the ring in Figure 9 to appear either brighter or dimmer compared to those in disks with finite cooling times (Zhang et al. 2023). This is because the angular momentum flux is not conserved in locally isothermal disks, as the waves exchange angular momentum with the local disk as they propagate (Miranda & Rafikov 2019).

##### 4.2.2. Vortex Longevity

In a global disk, vortices generate asymmetric density waves on the two sides due to geometric effects, causing radial migration of the vortex similar to the Type





**Figure 5.** Azimuthally averaged surface density profiles for gas (top; left column in Figure 4) and dust (bottom; right column in Figure 4) at  $t = \tau_{20}$  (column 5 in Table 1). Models with a higher  $A_0$  feature a gas gap closer to the vortex (top), resulting in closer dust rings as well (bottom). The dust ring closer to the vortex in each pair (dust ring A; the dotted arrows in each dotted+solid pair) eventually moves into the vortex, as seen in Model A1.

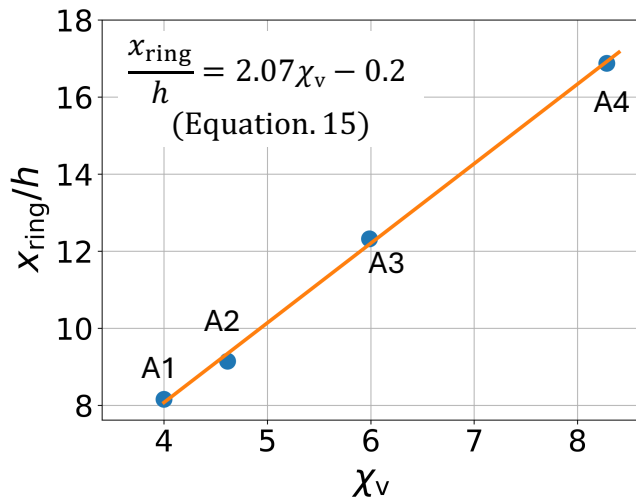


**Figure 6.** Empirical fitting between the aspect ratio of the vortex and the location of the dust ring.

I migration of planets (Paardekooper et al. 2010). The migration timescale is usually comparable to or longer than the disk lifetime unless the aspect ratio drops below 4 or the vortex exceeds a radial size of  $2h$ .

Relatively low viscosity ( $\alpha \lesssim 10^{-4}$ ) is required to sustain a long-lived vortex (Godon & Livio 1999; Fu et al. 2014). The high viscosity in hot disks can dampen the perturbations with small azimuthal mode numbers (Gholipour & Nejad-Asghar 2014). Observations from

ALMA infer low  $\alpha$  values for the disk, with upper limits ranging from  $10^{-4}$  to  $10^{-3}$ , suggesting that the maintenance of long-lived vortices is feasible in real disks (Pinte et al. 2023).

Radiative cooling can also impact the lifetime of the vortex. Fung & Ono (2021) found that the decay of the vortex is slow in both the isothermal and adiabatic limits, where the gas cooling time is much shorter or much longer than the vortex turnaround time.

RWI vortices exhibit vertical velocities in both 3D numerical simulations (Meheut et al. 2010) and linear calculations (Meheut et al. 2012c), with 3D growth rates comparable to those in 2D. Long-term simulations indicate that some RWI vortices can persist and grow over hundreds of years if the disk sustains the conditions that trigger RWI, such as dead zones (Meheut et al. 2012a). Nevertheless, elliptical instability can disrupt vortices with small aspect ratios ( $\chi \leq 4$ ) (Lesur & Papaloizou 2009; Richard et al. 2013) in 3D, whereas more elongated vortices behave comparably in both 3D and 2D scenarios.

Self-gravity inhibits long-lived vortex formation (Pierens & Lin 2018), but it may aid 3D vortices in resisting elliptical instabilities and extend their lifetime (Lin & Pierens 2018).

Dust-to-gas feedback might also impact vortex lifetime. When the dust-to-gas mass ratio surpasses 30% to 50% within the vortex, the dust feedback may excite dynamical instability and destroy the vortex (Fu et al. 2014; Crnkovic-Rubsamen et al. 2015).

Overall, various effects can either limit or extend vortex lifetimes. In more realistic scenarios involving multiple effects, vortex evolution and its corresponding disk interaction remain open areas for future research.

## 5. SUMMARY

We found that vortices can create dust rings and gaps in inviscid protoplanetary disks through shock dissipation of their induced density waves (Figure 1). By conducting 2D gas+dust simulations with varying vortex shapes, we established a linear correlation  $x_{\text{ring}}/h \sim 2.07\chi_v$  between vortex aspect ratio ( $\chi_v$ ) and dust ring location ( $x_{\text{ring}}$ ) (Equation 15; Figures 4 and 6). More elongated vortices generate density waves that carry less angular momentum flux (AMF), producing rings at larger separations.

In comparison to planet-disk interactions, we found that vortex-induced density waves carry over two orders of magnitude more AMF than planet-induced waves

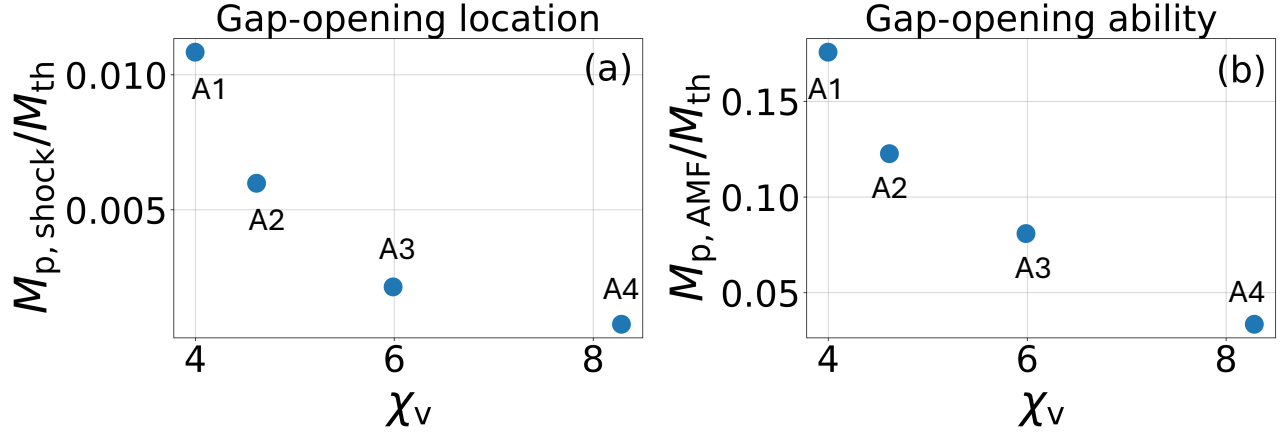


**Figure 7.** Panel (a): Correlation between vortex aspect ratio and planet mass for the planets whose waves shock at the same distance as the vortex-induced ones (See §3.4). (b): Correlation between vortex aspect ratio and planet mass for the planets whose waves carry the same amount of AMF as the vortex-induced ones (See §3.4).

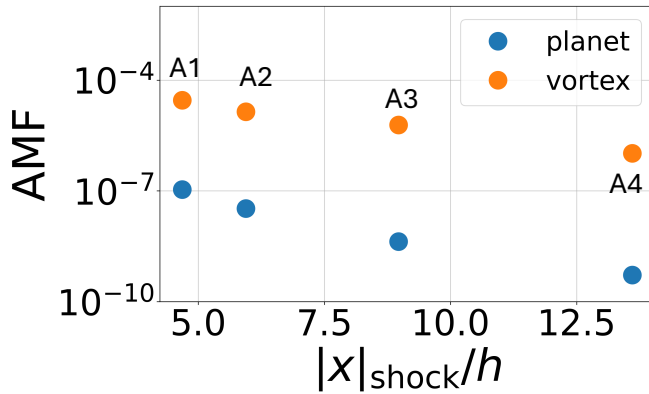


**Figure 8.** AMF carried by the planet-induced waves (blue dots) and vortex-induced waves (orange dots) that shock at the same distance.

with the same shock length, making vortices significantly more effective at gap opening (Figure 7).

Our study introduces a novel, non-planetary mechanism for the formation of rings and gaps in protoplanetary disks via vortex-disk interactions. Further research in more realistic disk environments is crucial to refine our understanding of this new mechanism.

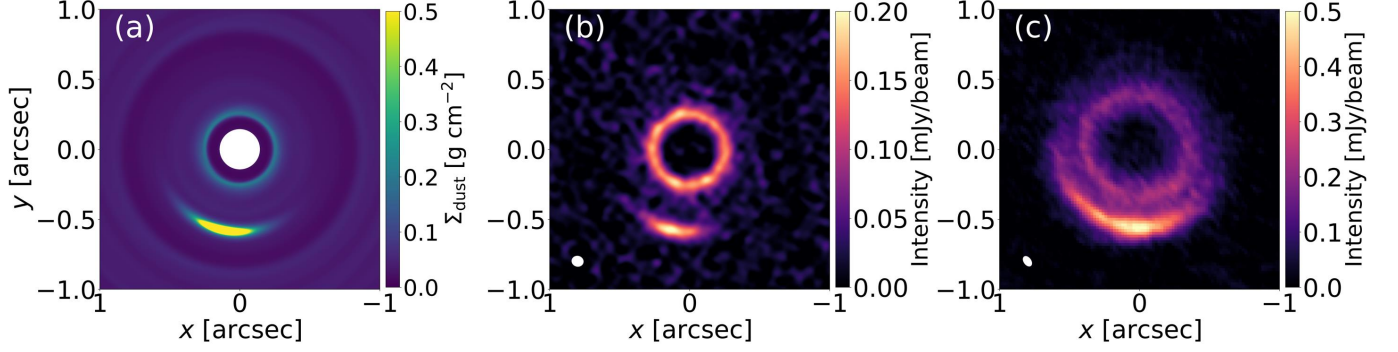
#### ACKNOWLEDGEMENTS

We are grateful to an anonymous referee for constructive suggestions that improved our paper. We would like to thank Doug Johnstone, Jeffrey Fung, Josh Calicino, Gianluigi Bodo, Gregory Herczeg, Haochang Jiang, Kengo Tomida, Min-Kai Lin, Nienke van der Marel, Roman Rafikov, Rixin Li and Tomohiro Ono for their comments and suggestions. We appreciate the Chinese Center for Advanced Science and Technology for hosting the Protoplanetary Disk and Planet Formation Summer School in 2022, organized by Xue-ning Bai and Ruobing Dong, which facilitated this research. X.M., P.H., and R.D. acknowledge the support of the Natural Sciences and Engineering Research Council of Canada (NSERC) [RGPIN-2023-05299], and the Alfred P. Sloan Foundation. P. H. acknowledges the financial support from NSERC ALLRP 577027-22. This research was enabled in part by support provided by the Digital Research Alliance of Canada [alliance.can.ca](http://alliance.can.ca).

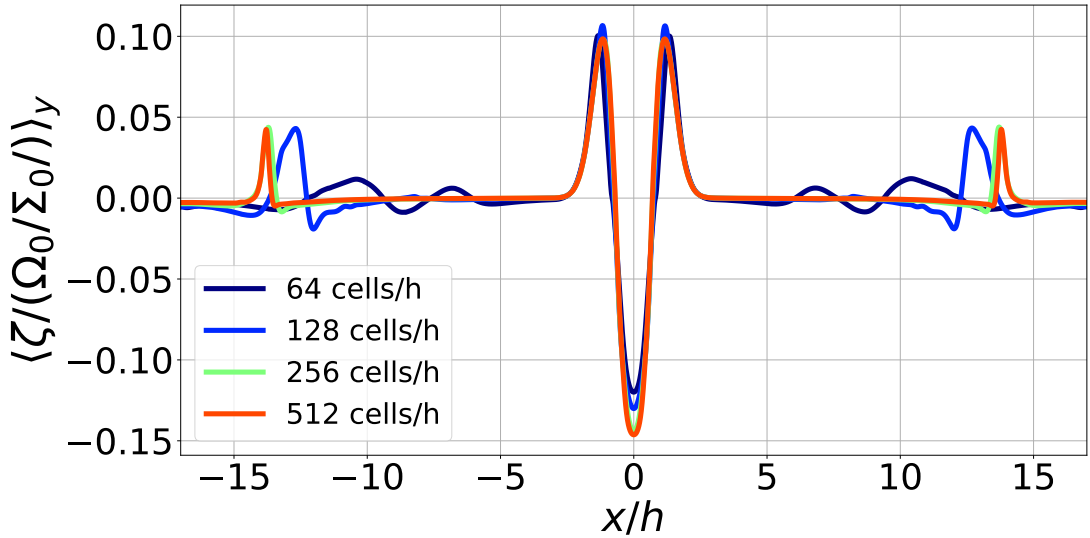
#### APPENDIX

##### A. CONVERGENCE TEST IN VORTENSITY

To confirm if a long-lived vortex can produce substructures through shock dissipation of density waves, it is crucial for our simulations to have sufficient resolution to capture the shock location, which is identified by peaks in vortensity (§3.2). Achieving convergence in vortensity is therefore essential for our goal.



**Figure 9.** Panel (a): Dust surface density from the global simulation for the disk Model A2. (b): The corresponding synthetic continuum image at 1.9 mm. The white ellipse in the bottom left corner represents the synthetic beam size of  $0.079'' \times 0.070''$ . (c): Continuum observations for HD135344B at 1.9 mm (Cazzoletti et al. 2018). The white ellipse in the bottom left corner indicates the beam size of  $0.076'' \times 0.047''$ .



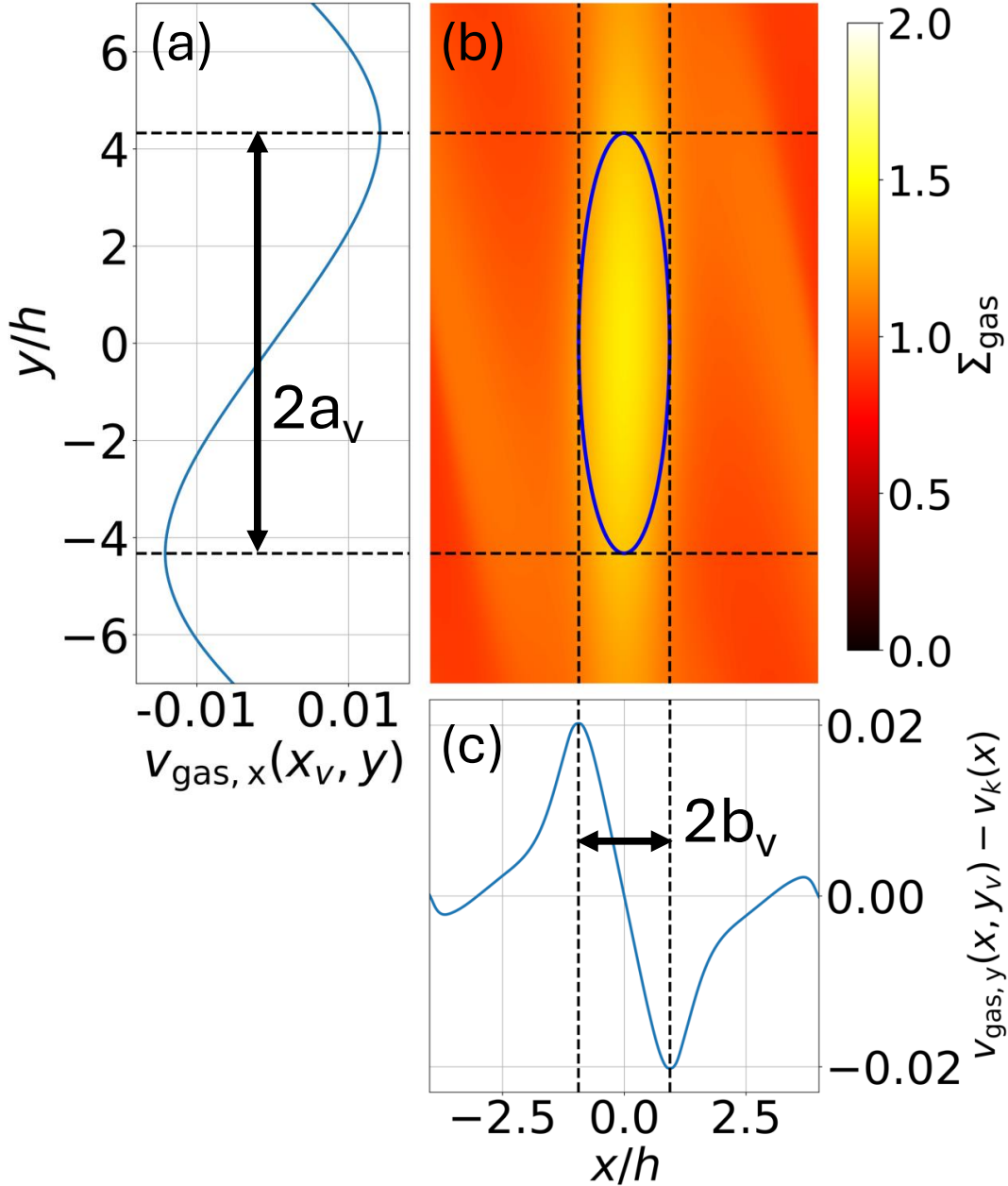
**Figure 10.** Vortensity radial profile at  $t = 360$  orbits for Model A4 is shown at resolutions of 64, 128, 256 and 512 cells/h.

Figure 10 illustrates the radial profiles of vortensity for Model A4 at various resolutions: 64, 128, 256, and 512 cells/h. We find that the location of the vortensity peaks converged at 256 cells/h. Thus, 256 cells/h is adequate for our simulations and analysis.

## B. VORTEX SHAPE

The shape of the vortex is characterized by its aspect ratio,  $\chi_v = a_v/b_v$ . The semi-major ( $b_v$ ) and semi-minor axis ( $a_v$ ) of the vortex core are calculated from velocity profiles ( $v_{\text{gas},y}(x, y_v) - v_k(x)$ ,  $v_{\text{gas},x}(x_v, y)$ ) near the vortex ( $x_v, y_v$ ), where  $v_k(x)$  is Keplerian velocity.

Figure 11 shows these velocity profiles for Model A4 at  $t = \tau_{20}$ . Both profiles converge to zero at the vortex center and exhibit variations with distance from the vortex center, attaining their local extremes near the edge of the vortex core. Hence,  $a_v$  and  $b_v$  is estimated as half the distance between two extremas in  $v_{\text{gas},y}(x, y_v) - v_k(x)$  and  $v_{\text{gas},x}(x_v, y)$ , respectively. The vortex in Figure 11 exhibits an aspect ratio of  $\chi_v = 4.61$ .



**Figure 11.** Radial velocity  $v_{\text{gas},x}$  along the  $y$  direction (a), surface gas density (b), and azimuthal velocity deviation from Keplerian velocity  $v_{\text{gas},y} - v_k$  along the  $x$  direction (c) for **Model A2** at  $t = \tau_{20}$ . Black dashed lines mark local extrema near the vortex. The distance between local maximum and minimum in  $v_{\text{gas},x}$  defines the semi-major axis  $a_v$ , while for  $v_{\text{gas},y} - v_k$  it defines the semi-minor axis  $b_v$ . An ellipse, delineated by  $a_v$  and  $b_v$  from the velocity profile, represents the vortex shape in blue.

## C. SYNTHETIC OBSERVATIONS

### C.1. Simulation

We use the grid-based hydrodynamics code Athena++ to conduct 2D global simulations in polar coordinates  $(r, \phi)$  for generating synthetic images. We consider the equation of state of the gas to be locally isothermal, where the radial profile of temperature is  $T(r) \propto (r/r_0)^{-0.5}$ , where  $r_0 = 65$  AU. The corresponding radial profile for the scale height of the gas disk  $h$  is  $h/r = 0.1(r/r_0)^{0.25}$ . Here,  $h = c_s/\Omega$ , where  $c_s$  is the sound speed. We introduce viscosity with  $\alpha = 10^{-5}$  (Shakura & Sunyaev 1973), and incorporate dust diffusion into the simulations.



To trigger RWI, we impose the pressure bump defined in Equation 8 at  $1.5 r_0$  using the parameters of Model A2. The background density follows a power law,  $\Sigma_{\text{gas}}(t = 0) = \Sigma_{\text{gas},0}(r/r_0)^{-0.5}$ , where  $\Sigma_{\text{gas},0} = 5.7 \text{ g cm}^{-2}$ . The total disk mass is  $0.06 M_{\odot}$ .

Our simulation domain spans  $0.1 r_0$  to  $3.2 r_0$  radially with constant logarithmic spacing and covers  $0$  to  $2\pi$  uniformly in the azimuthal direction. We employ a root mesh grid of  $62 \times 192$ , with level 4 refinement between  $0.25 r_0$  and  $2.5 r_0$  near the vortex to capture density wave evolution. Each level of refinement doubles the resolution, so the resolution in the radial direction at  $r_0$  reaches 33 cells per gas scale height at the finest grids.

The initial velocities are set by hydrostatic equilibrium for gas. Small velocity perturbations in white noise with an amplitude of  $0.01c_s$  are added in both radial and azimuthal directions to induce instability.

We model one dust species with  $St = 0.01$ , with an initial uniform dust-to-gas ratio of 0.01. At  $t = 0$  and  $r = r_0$ ,  $s = 0.3 \text{ mm}$  for  $\rho_{\text{m,dust}} = 1.2 \text{ g cm}^{-3}$ . To prevent rapid inward drift at the start of the simulation, dust motion begins at  $t = 200$  orbits.

Periodic boundary conditions are enforced along the  $\phi$  direction, while the radial boundary condition is kept fixed to the initial condition, following the damping zone described by Equation 12 with a damping rate of  $\zeta_{\text{dr}} = 1$ . The damping edge is calculated as  $1.3^{-2/3}x_{\text{max}}$  for the outer boundary and  $2.0^{2/3}x_{\text{min}}$  for the inner boundary.

## C.2. Radiative Transfer and Synthetic Observations

We follow the procedure outlined in (Huang et al. 2020) to post-process the outputs of 2D hydrodynamic global simulation, using the radiation transfer code RADMC-3D <sup>3</sup>(Dullemond et al. 2012) and the Common Astronomy Software Application (CASA) <sup>4</sup>(The CASA Team et al. 2022). The simulation is initialized using the stellar parameters of the disk HD 135344B (van der Marel et al. 2016), assuming the central star is a luminous blackbody sphere with  $R_{\star} = 2.2 R_{\odot}$ ,  $M_{\star} = 1.6 M_{\odot}$  and  $T = 6590 \text{ K}$ .

As RADMC-3D reads 3D density distributions instead of surface densities, we convert the output 2D surface densities to 3D density distributions using the following profile, assuming hydrostatic equilibrium for a vertically isothermal disk (Armitage 2020):

$$\rho(r, \phi, z) = \frac{1}{\sqrt{2\pi}} \frac{\Sigma(r, \phi)}{h(r)} e^{-z^2/2h(r)^2} \quad (\text{C1})$$

Here we consider two kinds of dust. Submicron-sized dust particles scatter and absorb stellar light at the disk surface. These dust particles are well-coupled with gas with a constant dust-to-gas of 0.01 and the same scale height as gas.

We obtain the disk temperature using `mctherm` from RADMC-3D, assuming the temperature is primarily influenced by sub-micron-sized dust particles. The dust opacity input for RADMC-3D is computed using `optool`<sup>5</sup> (Dominik et al. 2021), employing the DSHARP composition (Birnstiel et al. 2018) and a power-law dust size distribution given by  $n(a) \propto a^{-3.5}$ , where  $a$  represents the grain size. The minimum grain size considered is  $0.01 \mu\text{m}$ , while the maximum grain size is set to  $100 \mu\text{m}$ . Additionally, we assume that the dust grains are solid spheres without any porosity.

The dust emission at a wavelength of  $1.9 \text{ mm}$  is determined by utilizing  $0.3 \text{ mm}$  dust from the hydrodynamic simulation through ray-tracing in RADMC-3D. The dust surface density from the hydrodynamic simulation is converted to 3D dust density distribution using Equation C1, assuming the dust scale height to be 10% of the gas scale height. The opacity of  $0.3 \text{ mm}$  dust is also computed by employing the DSHARP composition (Birnstiel et al. 2018). Additionally, we include the effect of dust scattering in our computations.

To simulate the ALMA observation, we process the noise-free image from RADMC-3D using `simobserve` in CASA to incorporate observational noise and convolve it with the appropriate beam size. We adopt the ALMA configuration

<sup>3</sup> <https://www.ita.uni-heidelberg.de/~dullemond/software/radmc-3d/>

<sup>4</sup> <https://casa.nrao.edu/>

<sup>5</sup> <https://github.com/cdominik/optool>

of C4.8, similar to the real observation of HD 135344B (Cazzoletti et al. 2018), resulting in a synthetic beam size of  $0.079'' \times 0.070''$ . The synthetic image is generated with an integration time of 2 hours.

## REFERENCES

- ALMA Partnership, Brogan, C. L., Pérez, L. M., et al. 2015, *ApJL*, 808, L3, doi: [10.1088/2041-8205/808/1/L3](https://doi.org/10.1088/2041-8205/808/1/L3)
- Andrews, S. M., Huang, J., Pérez, L. M., et al. 2018, *ApJL*, 869, L41, doi: [10.3847/2041-8213/aaf741](https://doi.org/10.3847/2041-8213/aaf741)
- Armitage, P. J. 2020, *Astrophysics of Planet Formation*, 2nd edn. (Cambridge University Press)
- Asensio-Torres, R., Henning, T., Cantalloube, F., et al. 2021, *A&A*, 652, A101, doi: [10.1051/0004-6361/202140325](https://doi.org/10.1051/0004-6361/202140325)
- Bae, J., Isella, A., Zhu, Z., et al. 2023, in *Astronomical Society of the Pacific Conference Series*, Vol. 534, *Protostars and Planets VII*, ed. S. Inutsuka, Y. Aikawa, T. Muto, K. Tomida, & M. Tamura, 423, doi: [10.48550/arXiv.2210.13314](https://doi.org/10.48550/arXiv.2210.13314)
- Bae, J., Pinilla, P., & Birnstiel, T. 2018, *ApJL*, 864, L26, doi: [10.3847/2041-8213/aadd51](https://doi.org/10.3847/2041-8213/aadd51)
- Bae, J., & Zhu, Z. 2018, *ApJ*, 859, 118, doi: [10.3847/1538-4357/aabf8c](https://doi.org/10.3847/1538-4357/aabf8c)
- Baruteau, C., & Zhu, Z. 2016, *Monthly Notices of the Royal Astronomical Society*, 458, 39273941, doi: [10.1093/mnras/stv2527](https://doi.org/10.1093/mnras/stv2527)
- Birnstiel, T., Dullemond, C. P., & Pinilla, P. 2013, *A&A*, 550, L8, doi: [10.1051/0004-6361/201220847](https://doi.org/10.1051/0004-6361/201220847)
- Birnstiel, T., Dullemond, C. P., Zhu, Z., et al. 2018, *The Astrophysical Journal Letters*, 869, L45, doi: [10.3847/2041-8213/aaf743](https://doi.org/10.3847/2041-8213/aaf743)
- Casassus, S., van der Plas, G. M., Perez, S., et al. 2013, *Nature*, 493, 191, doi: [10.1038/nature11769](https://doi.org/10.1038/nature11769)
- Cazzoletti, P., van Dishoeck, E. F., Pinilla, P., et al. 2018, *Astronomy and Astrophysics*, 619, A161, doi: [10.1051/0004-6361/201834006](https://doi.org/10.1051/0004-6361/201834006)
- Cimerman, N. P., & Rafikov, R. R. 2021, *Monthly Notices of the Royal Astronomical Society*, 508, 23292349, doi: [10.1093/mnras/stab2652](https://doi.org/10.1093/mnras/stab2652)
- Crnkovic-Rubsamen, I., Zhu, Z., & Stone, J. M. 2015, *MNRAS*, 450, 4285, doi: [10.1093/mnras/stv828](https://doi.org/10.1093/mnras/stv828)
- Dominik, C., Min, M., & Tazaki, R. 2021, *OpTool: Command-line driven tool for creating complex dust opacities*, *Astrophysics Source Code Library*, record ascl:2104.010
- Dong, R., Li, S., Chiang, E., & Li, H. 2017, *ApJ*, 843, 127, doi: [10.3847/1538-4357/aa72f2](https://doi.org/10.3847/1538-4357/aa72f2)
- Dong, R., Rafikov, R. R., & Stone, J. M. 2011a, *ApJ*, 741, 57, doi: [10.1088/0004-637X/741/1/57](https://doi.org/10.1088/0004-637X/741/1/57)
- Dong, R., Rafikov, R. R., Stone, J. M., & Petrovich, C. 2011b, *ApJ*, 741, 56, doi: [10.1088/0004-637X/741/1/56](https://doi.org/10.1088/0004-637X/741/1/56)
- Dong, R., Zhu, Z., & Whitney, B. 2015, *The Astrophysical Journal*, 809, 93, doi: [10.1088/0004-637x/809/1/93](https://doi.org/10.1088/0004-637x/809/1/93)
- Dullemond, C. P., Juhasz, A., Pohl, A., et al. 2012, *RADMC-3D: A multi-purpose radiative transfer tool*, *Astrophysics Source Code Library*, record ascl:1202.015
- Fu, W., Li, H., Lubow, S., & Li, S. 2014, *ApJL*, 788, L41, doi: [10.1088/2041-8205/788/2/L41](https://doi.org/10.1088/2041-8205/788/2/L41)
- Fung, J., & Ono, T. 2021, *The Astrophysical Journal*, 922, 13, doi: [10.3847/1538-4357/ac1d4e](https://doi.org/10.3847/1538-4357/ac1d4e)
- Fung, J., Shi, J.-M., & Chiang, E. 2014, *The Astrophysical Journal*, 782, 88, doi: [10.1088/0004-637x/782/2/88](https://doi.org/10.1088/0004-637x/782/2/88)
- Gholipour, M., & Nejad-Asghar, M. 2014, *Monthly Notices of the Royal Astronomical Society*, 441, 19101915, doi: [10.1093/mnras/stu697](https://doi.org/10.1093/mnras/stu697)
- Godon, P., & Livio, M. 1999, *ApJ*, 523, 350, doi: [10.1086/307720](https://doi.org/10.1086/307720)
- Goodman, J., & Rafikov, R. R. 2001, *ApJ*, 552, 793, doi: [10.1086/320572](https://doi.org/10.1086/320572)
- Huang, P., & Bai, X.-N. 2022, *The Astrophysical Journal Supplement Series*, 262, 11, doi: [10.3847/1538-4365/ac76cb](https://doi.org/10.3847/1538-4365/ac76cb)
- Huang, P., Dong, R., Li, H., Li, S., & Ji, J. 2019, *The Astrophysical Journal Letters*, 883, L39, doi: [10.3847/2041-8213/ab40c4](https://doi.org/10.3847/2041-8213/ab40c4)
- Huang, P., Li, H., Isella, A., et al. 2020, *The Astrophysical Journal*, 893, 89, doi: [10.3847/1538-4357/ab8199](https://doi.org/10.3847/1538-4357/ab8199)
- Jiang, H., & Ormel, C. W. 2021, *Monthly Notices of the Royal Astronomical Society*, 505, 11621179, doi: [10.1093/mnras/stab1278](https://doi.org/10.1093/mnras/stab1278)
- Kevlahan, N. K. R. 1997, *Journal of Fluid Mechanics*, 341, 371, doi: [10.1017/S0022112097005752](https://doi.org/10.1017/S0022112097005752)
- Lesur, G., & Papaloizou, J. C. B. 2009, *Astronomy and Astrophysics*, 498, 112, doi: [10.1051/0004-6361/200811577](https://doi.org/10.1051/0004-6361/200811577)
- Li, H., Colgate, S. A., Wendroff, B., & Liska, R. 2001, *ApJ*, 551, 874, doi: [10.1086/320241](https://doi.org/10.1086/320241)
- Li, H., Finn, J. M., Lovelace, R. V. E., & Colgate, S. A. 2000, *ApJ*, 533, 1023, doi: [10.1086/308693](https://doi.org/10.1086/308693)
- Li, H., Li, S., Koller, J., et al. 2005, *ApJ*, 624, 1003, doi: [10.1086/429367](https://doi.org/10.1086/429367)
- Lin, D. N. C., & Papaloizou, J. 1986, *ApJ*, 309, 846, doi: [10.1086/164653](https://doi.org/10.1086/164653)

- Lin, M.-K., & Pierens, A. 2018, *Monthly Notices of the Royal Astronomical Society*, 478, 575591, doi: [10.1093/mnras/sty947](https://doi.org/10.1093/mnras/sty947)
- Lodato, G., Dipierro, G., Ragusa, E., et al. 2019, *MNRAS*, 486, 453, doi: [10.1093/mnras/stz913](https://doi.org/10.1093/mnras/stz913)
- Long, F., Pinilla, P., Herczeg, G. J., et al. 2018, *The Astrophysical Journal*, 869, 17, doi: [10.3847/1538-4357/aae8e1](https://doi.org/10.3847/1538-4357/aae8e1)
- Lovelace, R. V. E., Li, H., Colgate, S. A., & Nelson, A. F. 1999, *ApJ*, 513, 805, doi: [10.1086/306900](https://doi.org/10.1086/306900)
- Masset, F. 2000, *A&AS*, 141, 165, doi: [10.1051/aas:2000116](https://doi.org/10.1051/aas:2000116)
- Meheut, H. 2013a, in *European Physical Journal Web of Conferences*, Vol. 46, European Physical Journal Web of Conferences, 03001, doi: [10.1051/epjconf/20134603001](https://doi.org/10.1051/epjconf/20134603001)
- Meheut, H. 2013b, in *Poster presented at Protostars and Planets VI*
- Meheut, H., Casse, F., Varniere, P., & Tagger, M. 2010, *Astronomy and Astrophysics*, 516, A31, doi: [10.1051/0004-6361/201014000](https://doi.org/10.1051/0004-6361/201014000)
- Meheut, H., Keppens, R., Casse, F., & Benz, W. 2012a, *A&A*, 542, A9, doi: [10.1051/0004-6361/201118500](https://doi.org/10.1051/0004-6361/201118500)
- Meheut, H., Lovelace, R. V. E., & Lai, D. 2013, *MNRAS*, 430, 1988, doi: [10.1093/mnras/stt022](https://doi.org/10.1093/mnras/stt022)
- Meheut, H., Meliani, Z., Varniere, P., & Benz, W. 2012b, *A&A*, 545, A134, doi: [10.1051/0004-6361/201219794](https://doi.org/10.1051/0004-6361/201219794)
- Meheut, H., Yu, C., & Lai, D. 2012c, *MNRAS*, 422, 2399, doi: [10.1111/j.1365-2966.2012.20789.x](https://doi.org/10.1111/j.1365-2966.2012.20789.x)
- Miranda, R., Li, H., Li, S., & Jin, S. 2017, *The Astrophysical Journal*, 835, 118, doi: [10.3847/1538-4357/835/2/118](https://doi.org/10.3847/1538-4357/835/2/118)
- Miranda, R., & Rafikov, R. R. 2019, *The Astrophysical Journal Letters*, 878, L9, doi: [10.3847/2041-8213/ab22a7](https://doi.org/10.3847/2041-8213/ab22a7)
- Miranda, R., & Rafikov, R. R. 2020, *ApJ*, 892, 65, doi: [10.3847/1538-4357/ab791a](https://doi.org/10.3847/1538-4357/ab791a)
- Muto, T., Suzuki, T. K., & Inutsuka, S.-i. 2010, *ApJ*, 724, 448, doi: [10.1088/0004-637X/724/1/448](https://doi.org/10.1088/0004-637X/724/1/448)
- Narayan, R., Goldreich, P., & Goodman, J. 1987, *MNRAS*, 228, 1, doi: [10.1093/mnras/228.1.1](https://doi.org/10.1093/mnras/228.1.1)
- Ono, T., Muto, T., Takeuchi, T., & Nomura, H. 2016, *The Astrophysical Journal*, 823, 84, doi: [10.3847/0004-637x/823/2/84](https://doi.org/10.3847/0004-637x/823/2/84)
- Ono, T., Muto, T., Tomida, K., & Zhu, Z. 2018, *The Astrophysical Journal*, 864, 70, doi: [10.3847/1538-4357/aad54d](https://doi.org/10.3847/1538-4357/aad54d)
- Paardekooper, S.-J., Lesur, G., & Papaloizou, J. C. B. 2010, *The Astrophysical Journal*, 725, 146158, doi: [10.1088/0004-637x/725/1/146](https://doi.org/10.1088/0004-637x/725/1/146)
- Pérez, L. M., Benisty, M., Andrews, S. M., et al. 2018, *ApJL*, 869, L50, doi: [10.3847/2041-8213/aaf745](https://doi.org/10.3847/2041-8213/aaf745)
- Pierens, A., & Lin, M.-K. 2018, *Monthly Notices of the Royal Astronomical Society*, doi: [10.1093/mnras/sty1314](https://doi.org/10.1093/mnras/sty1314)
- Pinilla, P., Benisty, M., & Birnstiel, T. 2012, *Astronomy and Astrophysics*, 545, A81, doi: [10.1051/0004-6361/201219315](https://doi.org/10.1051/0004-6361/201219315)
- Pinte, C., Teague, R., Flaherty, K., et al. 2023, in *Astronomical Society of the Pacific Conference Series*, Vol. 534, *Protostars and Planets VII*, ed. S. Inutsuka, Y. Aikawa, T. Muto, K. Tomida, & M. Tamura, 645, doi: [10.48550/arXiv.2203.09528](https://doi.org/10.48550/arXiv.2203.09528)
- Richard, S., Barge, P., & Le Dizès, S. 2013, *A&A*, 559, A30, doi: [10.1051/0004-6361/201322175](https://doi.org/10.1051/0004-6361/201322175)
- Segura-Cox, D. M., Schmiedeke, A., Pineda, J. E., et al. 2020, *Nature*, 586, 228, doi: [10.1038/s41586-020-2779-6](https://doi.org/10.1038/s41586-020-2779-6)
- Shakura, N. I., & Sunyaev, R. A. 1973, *A&A*, 24, 337
- Sierra, A., Lizano, S., Mac í as, E., et al. 2019, *The Astrophysical Journal*, 876, 7, doi: [10.3847/1538-4357/ab1265](https://doi.org/10.3847/1538-4357/ab1265)
- Stone, J. M., & Gardiner, T. A. 2010, *ApJS*, 189, 142, doi: [10.1088/0067-0049/189/1/142](https://doi.org/10.1088/0067-0049/189/1/142)
- Stone, J. M., Tomida, K., White, C. J., & Felker, K. G. 2020, *The Astrophysical Journal Supplement Series*, 249, 4, doi: [10.3847/1538-4365/ab929b](https://doi.org/10.3847/1538-4365/ab929b)
- The CASA Team, Bean, B., Bhatnagar, S., et al. 2022, *Publications of the Astronomical Society of the Pacific*, 134, 114501, doi: [10.1088/1538-3873/ac9642](https://doi.org/10.1088/1538-3873/ac9642)
- van der Marel, N., van Dishoeck, E. F., Bruderer, S., et al. 2016, *A&A*, 585, A58, doi: [10.1051/0004-6361/201526988](https://doi.org/10.1051/0004-6361/201526988)
- van der Marel, N., van Dishoeck, E. F., Bruderer, S., et al. 2013, *Science*, 340, 11991202, doi: [10.1126/science.1236770](https://doi.org/10.1126/science.1236770)
- van der Marel, N., Birnstiel, T., Garufi, A., et al. 2020, *The Astronomical Journal*, 161, 33, doi: [10.3847/1538-3881/abc3ba](https://doi.org/10.3847/1538-3881/abc3ba)
- Zhang, M., Huang, P., & Dong, R. 2023, *The dependence of the structure of planet-opened gaps in protoplanetary disks on radiative cooling.* <https://arxiv.org/abs/2310.11757>
- Zhang, S., Zhu, Z., Huang, J., et al. 2018, *ApJL*, 869, L47, doi: [10.3847/2041-8213/aaf744](https://doi.org/10.3847/2041-8213/aaf744)
- Zhu, Z., Stone, J. M., Rafikov, R. R., & Bai, X.-n. 2014, *ApJ*, 785, 122, doi: [10.1088/0004-637X/785/2/122](https://doi.org/10.1088/0004-637X/785/2/122)